CARBON 49 (2011) 1305–1317

available at www.sciencedirect.com

ScienceDirect

journal homepage: www.elsevier.com/locate/carbon

Micro-channel development and hydrogen adsorption properties in templated microporous carbons containing platinum nanoparticles

Yunxia Yang [a], Craig M. Brown [b], Chunxia Zhao [c], Alan L. Chaffee [d], Burke Nick [a], Dongyuan Zhao [e], Paul A. Webley [e,*], Jacob Schalch [f], Jason M. Simmons [b], Yun Liu [b,g], Jae-Hyuk Her [b,h,i], C.E. Buckley [j], Drew A. Sheppard [j]

[a] Earth Science and Resources Engineering, CSIRO, VIC 3168, Australia
[b] National Institute of Standards and Technology Centre for Neutron Research, 100 Bureau Drive, MS 6102, Gaithersburg, MD 20899, USA
[c] School of Materials Science and Engineering, Wuhan University of Technology, Hubei, Wuhan 430070, PR China
[d] School of Chemistry, Monash University, VIC 3168, Australia
[e] Department of Chemical Engineering, Monash University, Australia National Hydrogen Materials Alliance, VIC 3168, Australia
[f] Oberlin College, 70 N Professor St, Oberlin, OH 44074, USA
[g] Department of Chemical Engineering, University of Delaware, Newark, DE 19716, USA
[h] Department of Material Science and Engineering, University of Maryland, College Park, MD 20742, USA
[i] GE Global Research, Niskayuna, NY 12309 USA
[j] Department of Imaging and Applied Physics, Curtin University of Technology, GPO Box U 1987, Perth, 6845 WA, Australia

ARTICLE INFO

Article history:
Received 29 June 2010
Accepted 26 November 2010
Available online 1 December 2010

ABSTRACT

Ordered microporous carbons containing dispersed platinum nanoparticles were fabricated and chosen as suitable models to investigate micro-structure development and hydrogen transport properties of zeolite-templated carbons. X-ray photoelectron spectroscopy analysis revealed that the enhanced heat of adsorption is related to the narrow micro-channels templated from the zeolite and the presence of certain C—O groups on the carbon. The lack of a well-defined and intense rotational transition line and the persistent broad H_2 recoil spectrum in neutron scattering results suggests a distribution of binding sites. Most interestingly, hydrogen diffusion occurs on two time scales, consisting of a fast liquid-like jump diffusion on the timescale of picoseconds along with an even faster bulk-like diffusion. The liquid-like motion is characterized by a diffusion constant of $(2.1 \pm 0.3) \times 10^{-8}$ m^2/s with an activation energy of ca. 77 K; both values indicate somewhat lower mobility than similar dynamics of H_2 on nanotubes, activated carbon XC-72, or Grafoil, yet greater mobility than that of bulk liquid. These unusual characteristics for hydrogen in carbons are believed to arise from the network of narrow pores in this zeolite-templated image of the zeolite. In fact, the diffusion constants of the templated carbons are extremely similar to those measured for zeolite 13X.
© 2010 Elsevier Ltd. All rights reserved.

1. Introduction

Nanocasting has become an effective approach for controlling structural replication from hard templates in the micro- and meso-range. Many research groups have attempted to make well-defined micro-structures using this approach [1–4], especially with carbon [5–9]. However, constrained by the instrumental limits for detecting micro-pore structural

* *Corresponding author:* Fax: +61 3 9905 5686.
E-mail address: paul.webley@eng.monash.edu.au (P.A. Webley).
0008-6223/$ - see front matter © 2010 Elsevier Ltd. All rights reserved.
doi:10.1016/j.carbon.2010.11.050

regularities, there is a lack of fundamental understanding of the development of the micro-structure in these templated carbons. In our previous work [8], we focused on carbon structure development by templating and reported well-structured, microporous carbons containing well-dispersed Pt nanoparticles. The carbons developed were tested for their hydrogen storage capacities and very promising values were reported. Similar observations have been reported by other groups for carbons fabricated with similar methodologies but using alternative templates [10–12]. The hydrogen storage capacity was observed to be related to the pore size, high surface area and large micro-pore volume of the samples. However, due to the limited understanding of the structural properties of these carbons (e.g. carbon chemistry, pore geometries, accessibilities and connectivity), the relationship between hydrogen storage capacities, heat of adsorption and structural properties remains unclear.

In the present work, we simplified the fabrication procedure and controlled the carbon replication process by using acetylene gas as a single carbon precursor. Because the acetylene molecule is much smaller than that of furfuryl alcohol and propylene carbon precursors used in our previous work (which we refer to as the "2-step" procedure), improved gas diffusion into the pores of the templates is expected, so that only one chemical vapor deposition step is needed when infiltrating carbon into the Pt impregnated NaY zeolite templates (which we refer to as the "1-step" procedure).

A good dispersion of Pt nanoparticles is obtained in addition to much better controlled structural replication from the template. Therefore, this new structure is used as a model structure for investigating the micro-channel, pore geometry, connectivity, surface chemistry and gas accessibility in templated carbons. To this end, we have employed a combination of advanced analytical techniques such as neutron scattering, X-ray photoelectron spectroscopy (XPS), and small angle X-ray scattering (SAXS) as well as other traditional analyses. The results of these techniques are further correlated to the hydrogen storage properties observed in this work.

2. Experimental work

2.1. Synthesis

Microporous carbons were prepared according to the following procedure: (i) powdered zeolite NaY (CBV 100, ZEOLYST international with a Si/Al ca. 2.55) was added into an aqueous solution of Pt $[(NH_3)_4](NO_3)_2$ (99.9+%, Sigma Aldrich) with stirring to achieve incipient wetness impregnation. Parent templates are designated as 1%-PtY, 6%-PtY, and 40%-PtY; (ii) PtY templates were then dehydrated by heating to 400 °C with a slow ramping rate 5 K/min under inert nitrogen purge overnight and then cooled to room temperature; (iii) chemical vapor deposition (CVD) using acetylene (5.18 ± 0.1% in nitrogen) was then immediately carried out at 600 °C for 4 h, using a flow rate of approximately 400 ml/min. This was followed by heat treatment at 900 °C in inert argon gas for another 3 h to further strengthen the carbon structure. The samples produced from this stage are composite carbon samples; (iv) the template was then leached by immersing the composite sample in 48% hydrofluoric acid for 3 h, followed by washing and drying in a vacuum oven at 30 °C for 24 h. The final carbon products are denoted as x%Pt-Ac with x% referring to the Pt loading amount in the carbon and Ac referring to the carbon made from Acetylene gas precursor. In comparison, blank carbon is made in the same approach by using original zeolite without any Pt loading and denoted as 0%Pt-Ac.

2.2. Characterization

Powder X-ray diffraction (XRD) patterns were acquired using an X-ray diffractometer (Philips PW1130, CuK_α). Scanning electron microscopy (SEM) images were obtained on a JEOL FESEM 6300 at an accelerating voltage of 15 kV. Transmission electron microscope (TEM) images were recorded on a Philip model JEM 2011 and a Philips CM 20 electron microscope operated at 200 kV. Thermal gravimetric analyses (TGA) were carried out on a Mettler Toledo TGA/SDTA851. Nitrogen and hydrogen sorption measurements were performed on a Micromeritics ASAP 2020 volumetric adsorption analyzer equipped with a turbo-molecular pump. The samples were out-gassed under vacuum at 350 °C for 6 h prior to use. Hydrogen adsorption isotherms at 77 and 87 K were measured up to 1 bar. Specific surface areas were calculated by the Brunauer–Emmett–Teller (BET) method. Total pore volumes were taken at a relative pressure of $P/P_0 = 0.97$. Micro-pore volumes were calculated from the Dubinin–Radushkevich (DR) equation. Mesopore volume was determined by subtracting the micropore volume from the total pore volume. Pore size distributions were obtained using non-local density functional theory (DFT) (assuming cylindrical pore geometry) after using incremental dose of 5 ml/g STP for low pressure data acquisition. High-pressure sorption measurements on 0% and 1%Pt-Ac were performed on a home-built Sievert apparatus using scientific grade hydrogen [13]. Prior to measurement, the samples were degassed overnight at 200 °C using a turbo-molecular pump. Once degassed, the samples were loaded into the measurement cell inside a He glovebox.

Small angle X-ray data was acquired on a Bruker NanoSTAR using a wavelength of $\lambda = 1.5418$ Å (CuK_α) with a 2D multiwire detector. Data were recorded at a sample to detector distance of 23 and 65 cm, respectively. The raw data were radially averaged, background subtracted and put on an absolute scale by calibrating against a known standard via the method of Spalla et al. [14] Each sample was modeled using the unified fit approach with a data range of $0.01\ Å^{-1} < Q < 0.839\ Å^{-1}$ using the Irena 2 SAS modeling macros within the software package Igor Pro 6 (Wavemetrics, Oregon USA) [15–17]. The unified fit approach uses a multi level fitting method whereby each level is modeled using a Guinier region (particle size dependent scattering) and a power law region (surface scattering dependent). Further details on this modeling method are supplied in the Supporting Information.

X-ray photoelectron spectra were acquired on a Kratos AXIS Ultra DLD spectrometer with a monochromatic Al-Kα radiation source ($h\nu = 1486.6$ eV) operating at 150 W. High resolution core level spectra were acquired using a 20 eV pass energy and 0.1 eV step, while the survey spectra use a 160 eV pass energy and 1 eV step. A charge neutralization gun is used to minimize the effects of charging and all

binding energies are corrected to the aliphatic hydrocarbon component of the C1s peak (graphitic carbon in our case) at 285.0 eV. Shirley background and Voigt functional form have been used in spectra analysis.

Neutron scattering measurements were performed using the Filter-Analyzer Neutron Spectrometer (FANS) [18], the High-Flux Backscattering Spectrometer (HFBS) [19], and the Disc-Chopper Spectrometer (DCS) [20] at the National Institute of Standards and Technology (NIST) Center for Neutron Research (NCNR). FANS uses a pyrolytic graphite monochromator bracketed between two Söller collimators (of 20′ divergence before and after the monochromator) to produce a collimated, mono-energetic beam of neutrons, which is directed onto the sample. The energy transferred to the sample is determined by passing the scattered neutrons through a low-energy, band-pass filter consisting of polycrystalline Bi, Be, and graphite before reaching the ^{3}He detectors. The filter cut-off energy is about 1.8 meV with an energy resolution of 1.1 meV. The primary spectrometer contributes slightly to the resolution in the region around 15 meV so that the overall energy resolution is 1.2 meV. The HFBS spectrometer was operated in fixed-widow mode where the doppler drive is held stationary and the total intensity is recorded per detector as a function of temperature. Data were taken for the bare sample on cooling, and the 0%Pt-Ac loaded at 0.5 and 1.0 wt.% H_2 on cooling at a rate of 1 K/min. The DCS spectrometer was operated in medium resolution mode with an incident neutron wavelength of 5.0 Å, providing a full-width at half-maximum (FWHM) resolution of ca. 50 μ eV at the elastic channel. Quasi-elastic neutron scattering (QENS) data were collected over three banks of detectors and binned into groups for data analysis covering a mean elastic momentum transfer range of $0.27\ \text{Å}^{-1} < Q < 2.32\ \text{Å}^{-1}$. Data were collected at 30, 40, 50 and 60 K for both the bare material and 0.5 wt.% H_2-loaded 0%Pt-Ac. An instrumental resolution measurement of the bare material was performed at 10 K. Standard corrections were made and the bare data was subtracted from each loaded spectrum measured at the same temperature to generate the symmetrized scattering function, S(Q, ω).

For the neutron scattering experiments, the dehydrated 0%Pt-Ac (FANS: 561 mg; DCS: 1.33 g) or 1%Pt-Ac (675 mg) was transferred to a cylindrical aluminum cell equipped with a capillary gas line and valve, and sealed with an indium o-ring. The sample was mounted onto a sample stick, equipped with a stainless-steel gas line with an additional valve for use in a closed-cycle helium refrigerator (CCR). All sample transfers were performed in a helium-filled glove box equipped with water and oxygen monitors. Residual helium was pumped out of the room-temperature sample using a turbo-molecular pump prior to the experiments. For each hydrogen loading on FANS, the sample was first warmed to ca. 50 K and then a calculated amount of H_2 gas was loaded into a container of known volume at room temperature. The sample was then exposed to the hydrogen gas and after reaching equilibrium, the temperature was slowly cooled down to 4 K. The pressure gauge always read zero before the temperature reached 25 K indicating that all of the hydrogen was adsorbed. For HFBS and DCS, the H_2 gas was introduced in the sample cell at 70 K. For the QENS measurement on DCS, there was negligible vapor pressure recorded in the system when cooled to 60 K allowing for direct comparison of the data at all temperatures.

In general, for a system composed of immobile molecules along with translationally diffusing molecules, QENS data can be described in terms of the incoherent scattering function (1):

$$S_{\text{inc}}(Q,\omega) = \left(A_0(Q) + A_1(Q)\frac{\frac{\Gamma}{2}}{\pi}\frac{1}{\omega^2+\frac{\Gamma^2}{2}}\right) * \delta(Q,\omega), \quad (1)$$

where the elastic function is just the instrument resolution ($\delta(Q, \omega)$) modulated by an intensity ($A_0(Q)$) and the quasielastic feature, of intensity $A_1(Q)$, is a Lorentzian peak shape in energy transfer (ω) with full-width half-max, Γ. The stationary and mobile components and peak widths are dependent on the momentum transfer of the scattering and are convoluted with the instrument resolution function. If several diffusive motions are present in the system they are incorporated by adding further Lorentzians to the fit function before convolution. Data from the three spectrometers were reduced and fit to appropriate functions using available tools [21].

3. Results and discussion

3.1. *Electron microscopy*

3.1.1. *Structure development*

The morphologies of the microporous carbons are shown in Fig. SI1 (Supplementary Information), all revealing a more faithful morphology replication of the zeolite template than in the previous 2-step work.

Transmission electron microscopy (TEM) images (Fig. 1a–d) of the carbon samples without or with Pt loading all show very good crystal morphology retention from their parent templates. The high-resolution TEM images of the 1%Pt-Ac sample (Fig. 1(b)) show clear structural fringes that are constructed of micro-channels running in different directions. Fast Fourier transform (inset b of Fig. 1b) of the image gives transformed spots in three different directions, corresponding to three different *d*-spaces, $d_1 = 9$ Å, $d_2 = 12$ Å and $d_3 = 20$ Å, revealing a regular structure development in this carbon sample. Since such structure was not observed in the carbons developed in the 2-step work, it suggests that better controlled structural replication was indeed obtained with the current approach. Therefore, we are confident in choosing this carbon sample as the model structure for the consideration of pore geometry, accessibility and connectivity in templated carbons.

3.1.2. *Pt particle development*

Scanning electron microscopy (SEM, Fig. SI1) and TEM (Fig. 1) show a bimodal distribution of particle sizes in the Pt loaded samples. The smallest particles, on the order of 10–60 Å, are relatively uniformly dispersed. These are accompanied by particles whose average size increases with the amount of Pt salt added to the starting zeolites. For the 6%Pt-Ac sample, the large particles are on the order of ≈200 Å, while the 40%Pt-Ac sample shows particles that are ≈350 Å. These larger particles were not observed in the 40%Pt-C developed in the 2-step work with similar Pt loading [8]. Further, energy dispersive X-ray (EDX) results indicate that these larger

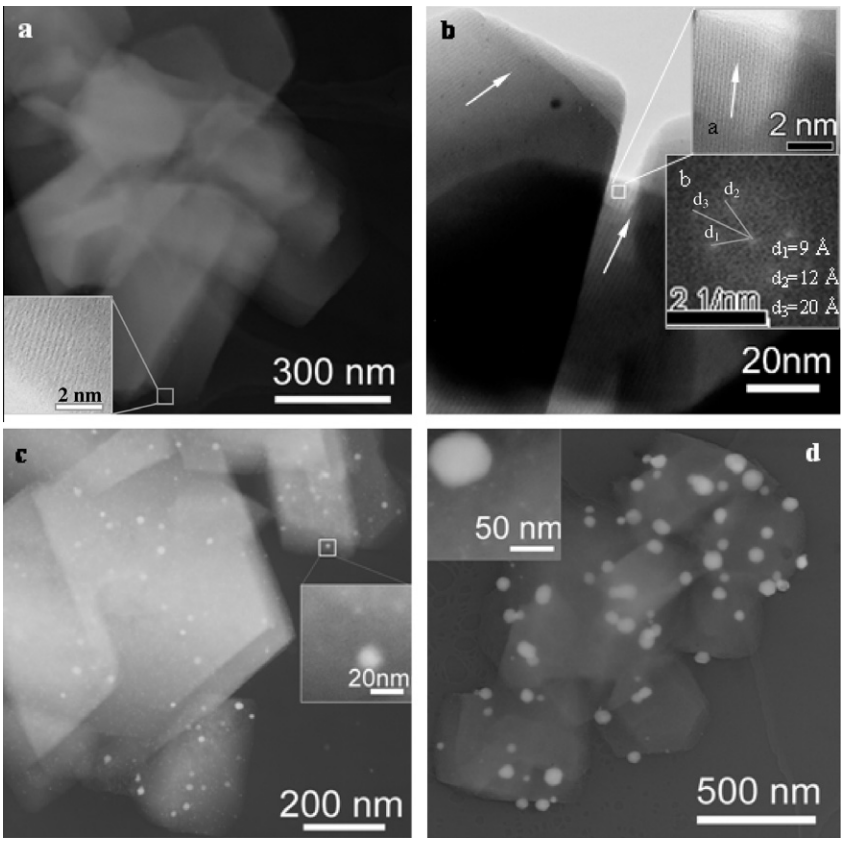

Fig. 1 – TEM images for the produced carbon samples: (a) 0%Pt-Ac with inset focusing on the zoomed area showing the fine fringes; additional lower resolution image for this sample is shown in Fig. SI2 (Supporting Information); (b) 1%Pt-Ac (arrows indicates the orientation of the fringes) with inset showing the fast Fourier transform of the zoomed area; (c) 6%Pt-Ac; (d) 40%Pt-Ac.

particles are Pt-dominant, suggesting that they are Pt nanoparticles encapsulated in carbon and that the carbon templating procedure used here has less control over metal dispersion than our previous 2-step procedure.

One possible explanation for this bimodal distribution is that there are two types of coordinated $Pt[NH_3]_4^{2+}$ ions in the parent zeolite framework after Pt-salt wetness impregnation. One type is the $Pt[NH_3]_4^{2+}$ ion which has undergone ion-exchange with the Y zeolite and replaced mainly the Na^+ ion locations. These ions have constrained mobility, resulting in slow migration during reduction, forming small, dispersed Pt nanoparticles. Meanwhile, during the wetness impregnation step, some Pt ions exist in the original salt-coordinated form $[Pt(NH_3)_4]^{2+}(NO_3)_2]$, likely both inside and outside of the zeolite framework. Compared to the ion-exchanged cations, $Pt[NH_3]_4^{2+}$ in the bulk salt has more freedom to transport and form aggregates during the heating and reduction process, leading to the development of larger Pt nanoparticles; the more Pt in the system, the more this alternative environment occurs and the greater the chance for agglomeration.

The reason why the more complex 2-step procedure produced superior Pt dispersion to the 1-step procedure is the use of furfuryl alcohol as one of the carbon precursors, which polymerizes during the intermediate heating period forming a cross-linked network. This network constrains the mobility of all of the Pt ions, resulting in slow migration of the metal ions during the heating and carbon deposition step and leading to the development of well-dispersed Pt nanoparticles. In the 1-step procedure, where no furfuryl alcohol was employed, no polymerization can occur during the heating period. Pt nanoparticles grow freely during carbon deposition from acetylene gas, resulting in the more random and bimodal size distribution of the Pt nanoparticles. Further corroborating evidence will be presented in the small-angle X-ray scattering (SAXS) analysis.

3.2. *Pore size distribution*

Pore sizes determined using nitrogen adsorption and BET analysis are concentrated below 2 nm with fluctuations around 5, 7–8, 12, and 20 Å (Fig. 2), indicating the carbon's microporous nature. These pore sizes correspond well with the *d*-spacings obtained from TEM for the 1%Pt-Ac sample (Fig. 1b), further confirming the structural regularity and development of micro-pore channel arrays in these samples as well as the effectiveness of the zeolite-templating. More detailed physical properties obtained from the nitrogen adsorption are summarized in Table 1.

3.3. *X-ray diffraction*

Wide-angle X-ray diffraction (XRD) patterns of 1%Pt-Ac, 6%Pt-Ac, 40%Pt-Ac show that broad Pt diffraction peaks are evident in the produced carbon samples (Fig. SI3), revealing the

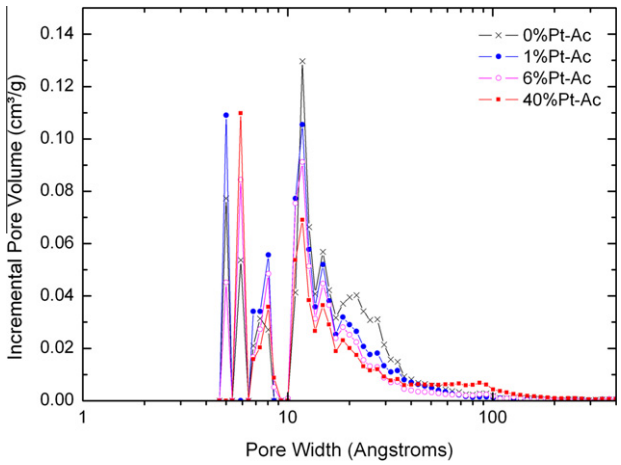

Fig. 2 – Pore size distribution of the carbons produced using a NLDFT analysis of nitrogen BET isotherms.

formation of Pt nano-crystalline particles. Pt nanoparticle sizes calculated from the Scherrer equation are about 10 Å for the 1%Pt-Ac sample, 100 Å for the 6%Pt-Ac sample, and 330 Å for the 40%Pt-Ac sample, each of which is similar to the sizes measured via electron microscopy. A weak feature at a scattering angle ca. 6° was observed in all of the carbons except the 40%Pt-Ac, which corresponds to a *d*-space of ≈14 Å and of similar dimension as the zeolite super cages and is an indication of the structural regularity that has been developed from the template. The reason that 40%Pt-Ac did not show a 6° diffraction peak is probably due to the loss of the structural regularity when Pt loading is too high. This is discussed further in the small angle analysis section.

3.4. *Small angle X-ray analysis*

Fig. 3a shows the measured SAXS data and the model fit for the blank 0%Pt-Ac sample. A broad peak is evident at scattering vector, Q, ca. 0.45 $Å^{-1}$, corresponding to a repeat distance of 14 Å, which originates from carbon replication of the packing structure of the largest NaY pore. For the 0%Pt-Ac sample, a 2-level unified fit model was employed. The high-Q data (level 1 of model) also employed a correlation function to account for the regularity of carbon spheres that were templated from the largest NaY zeolite pore [15,16]. From each level a size parameter (the radius of gyration, R_g) was extracted. This radius of gyration (the shoulder in the Q-range 0.07–0.4 $Å^{-1}$) can be due to scattering from the pores, the carbon or a combination of both if the pores and carbon are of similar size. There is no way to distinguish between them in this case. The R_g for level 1 was 10.4 ± 1.0 Å while the R_g for level 2 was 169 ± 17 Å. The exact relationship between R_g and a physically meaningful structure depends on the assumed shape of the structure. For example, assuming a spherical morphology, the diameter, *d*, is given by $d = 2\sqrt{5/3}R_g$. Therefore an R_g of 10.4 Å corresponds to spheres 26.9 Å in diameter. Without specific knowledge of the various scattering contributions, extracting a size from R_g is not possible with the current SAXS data. The R_g value of 169 Å for level 2 corresponds to spheres 436 Å in diameter or cuboids with side lengths of 338 Å [17]. In this case, we believe this R_g value was from the carbon cuboids with side lengths of 338 Å. Scattering from the mesopores can be excluded in this case as the spherical diameter calculated from R_g results in pores that are significantly larger than the average size measured using nitrogen adsorption. TEM shows that the 0%Pt-Ac has carbon particles that range in size from a few hundred angstroms up to several thousand angstroms in diameter. However, information from particles larger than ca. 630 Å is outside the Q-range of the instrument used.

The Pt-containing carbons were modeled (Fig. 3b–d) on the assumption that the scattering curves were comprised of scattering from the carbon and its pores as well as scattering from the Pt nanoparticles. From this, the following trends were observed: two sizes for the Pt particles could clearly be discerned, and increasing the Pt content had a negative effect on the carbon templating of the parent zeolite.

Assuming that the Pt particles are spherical, an approximation that is consistent with TEM imaging, we find that the 1%Pt-Ac is comprised of Pt particles with average diameters of 42 ± 4 Å and 148 ± 15 Å, respectively. The sizes of the Pt particles are in reasonable agreement with TEM given that SAXS collects data from sample volumes about 7 orders of magnitude larger than those for TEM, and hence determines a more representative average size of the physical clusters existing in the carbon matrix (Fig. SI2). The difference between the crystallite size determined from XRD and the 42 Å particle size derived from SAXS suggests that some of these Pt particles may in fact be polycrystalline. As the Pt content increases to 6 and 40% we see that the average diameter of Pt particles increases from 51 ± 5 Å and 180 ± 18 Å for the 6%Pt-Ac to 62 ± 6 Å and 207 ± 21 Å for the 40%Pt-Ac respectively. The dual Pt particle size of 6%Pt-Ac corresponds well to the diameter of Pt particles seen in TEM. TEM of 40%Pt-Ac shows Pt particles of ~50 Å (Fig. 1d, inset) and a number of particles ranging in size from 210 to 800 Å (the big dots in Fig. 1d). The smaller size corresponds well to the sizes derived

Table 1 – Surface area and pore volumes of carbons.

Samples	Pt loading (wt.%)	BET specific surface area (m^2/g)	Pore volume (cm^3/g)		H_2 uptake 77 K and 1 bar (wt.%)	H_2 uptake at 87 K and 1 bar (wt.%)
			V_{micro}	V_{meso}		
0%Pt-Ac	0	2200	0.94	0.27	1.7	1.5
1%Pt-Ac	1	2087	0.87	0.19	2	1.4
6%Pt-Ac	6	1930	0.8	0.15	1.6	1.2
40%Pt-Ac	40	912	0.43	0.05	–[a]	–[a]

[a] After sample transfers there was insufficient material for further hydrogen storage measurements.

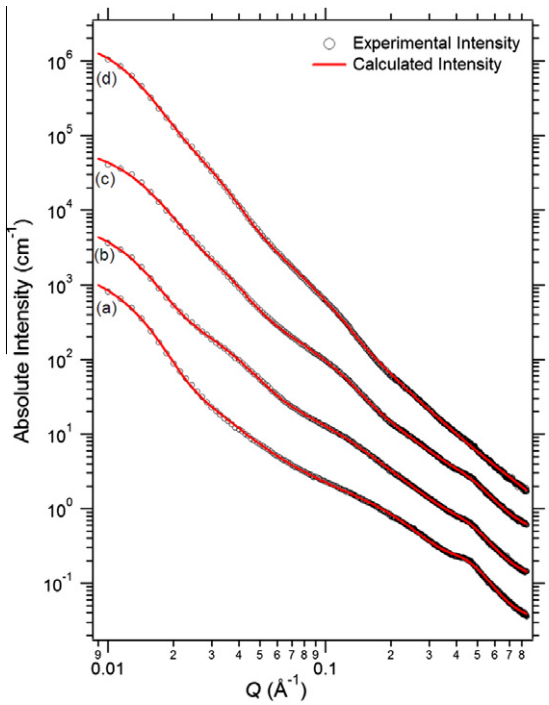

Fig. 3 – (a) Small angle X-ray scattering pattern of the blank 0%Pt-Ac (○) and the calculated scattering curve from the unified fit model (—). (b) Small angle X-ray scattering pattern of 1%Pt-Ac (○) and the calculated scattering curve from the unified fit model (—). (c) Small angle X-ray scattering pattern of 6%Pt-Ac (○) and the calculated scattering curve from the unified fit model (—). (d) Small angle X-ray scattering pattern of 40%Pt-Ac (○) and the calculated scattering curve from the unified fit model (—).

from SAXS. Scattering from Pt particles of 350–630 Å in size contribute to the SAXS scattering curve but their contribution is impossible to differentiate from the carbon support of similar size. Therefore, there is a size deviation for the bigger sized particles.

The increasing Pt content also has a negative impact on the templating (and porosity based on Fig. 2 and Table 1) of the carbon. The correlation function used in the modeling of high-Q data (the peak at Q = ca. 0.45 Å^{-1}) results in a *k* factor (Supporting Information, Eq. (3)) that is a measure of the regularity of the carbon spheres arising from templating the porosity of the zeolite parent material. For spheres (carbon spheres or spherical pores) arranged in a perfect face-centered cubic structure, the *k* factor has a value of 5.92 [16]. For the pure 0%Pt-Ac, the *k* factor has a value of 2.9 indicating moderate replication of the NaY pore structure. The *k* factor drops to 2.7 for 1%Pt-Ac and 2.3 for the 6% Pt sample respectively. This is in accord with our observation that the diffraction peak broadens and decreases in intensity before the peak disappears completely for the 40%Pt-Ac (the *k* factor is ca. 0). Comparison with the 0%Pt-Ac sample suggests that as the Pt loading increases, the Pt either fills the pore channels with deposited Pt or blocks the pore channels. This then denies access of the acetylene to the largest pores, resulting in decreased replication of the pore structure of the parent templates with a consequent decrease in surface area and pore volume (Table 1).

3.5. *Hydrogen adsorption isotherm and isosteric heat*

Hydrogen adsorption isotherms measured at 77 and 87 K are shown in Fig. 4a, all showing fully reversible adsorption, suggesting physical adsorption and no chemisorption. More detailed hydrogen adsorption data can be found in Table 1. Though 0%Pt-Ac has a slightly higher surface area compared to 1%Pt-Ac, 2200 versus 2087 m^2/g, the latter shows higher hydrogen adsorption capacity at 77 K and 1 bar pressure. However, it is evident from the excess adsorption isotherm up to 50 bar that the higher surface area 0%Pt-Ac exhibits a higher saturation hydrogen adsorption capacity at 50 bar compared to 1%Pt-Ac (Fig. 5).

Considering the pore size distribution in these two samples (Fig. 2), 1%Pt-Ac has somewhat smaller micro-pores than 0%Pt-Ac even though it has less total surface area. This observation is consistent with the previous finding that smaller pores and their enhanced binding energies affect the low pressure capacities more than larger micro- and mesopores, (more work related to this conclusion is provided in Fig. SI4). All else being equal, this leads to enhanced adsorption capacity at low pressures on the carbon samples having either the smallest micro-pores or simply more of the smallest micro-pores, even though they have less total surface area than those samples having bigger pores [7,22,23]. However, it is important to note that the presence of small pores is not a requirement for enhanced isosteric heats [24,25]; as we show below, surface chemistry may also play a role in affecting the heats of adsorption. With increased pressure, the smallest micro-pores become saturated and larger micro-pores and mesopores start affecting the hydrogen adsorption capacity, Fig. SI4 (Supporting Information). In the end, as observed by many other research groups, the final hydrogen adsorption capacity on a carbon sample at high pressure is still determined by the total micro- and mesopore volume or surface area of the sample.

Meanwhile, it is clear that increasing the Pt loading amount does not increase the hydrogen adsorption capacity. When Pt loading increases to 6%, a much reduced hydrogen adsorption capacity, about 1.6 wt.%, was observed compared to the 1%Pt-Ac (Table 1). Heats of adsorption, determined from the 1 bar hydrogen adsorption isotherms at 77 and 87 K using the Clausius–Clapeyron equation [8,11,12], are shown in Fig. 4b, with all of the samples' heat of adsorption showing a decreasing trend with increasing hydrogen loading. Compared to the blank 0%Pt-Ac carbon, enhanced heats of hydrogen adsorption were observed in both the 1%Pt-Ac and 6%Pt-Ac samples. 1%Pt-Ac sample exhibits the highest heat of adsorption which coincides with the highest adsorption capacity at 1 bar and 77 K, while 6%Pt-Ac has higher heat of adsorption than 0%Pt-Ac but much less micro-pore volume and lower hydrogen adsorption capacity, suggesting that the increase in the heat of adsorption is not enough to offset the influence by the decreased micro-pore volume for hydrogen adsorption.

Considering the fact that these two Pt-containing samples have less surface area and micro-pore volume, as probed by nitrogen, than the blank carbon, the hypothesis of field

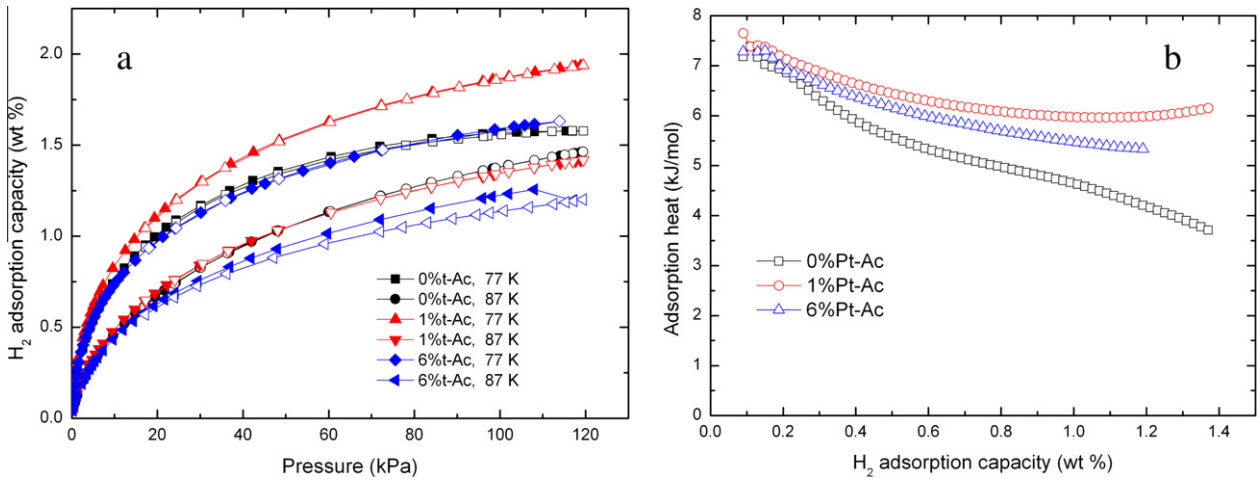

Fig. 4 – (a) Hydrogen adsorption isotherms and (b) heats of hydrogen adsorption on the carbons. In panel a, adsorption data are shown as filled symbols and desorption is shown as open symbols.

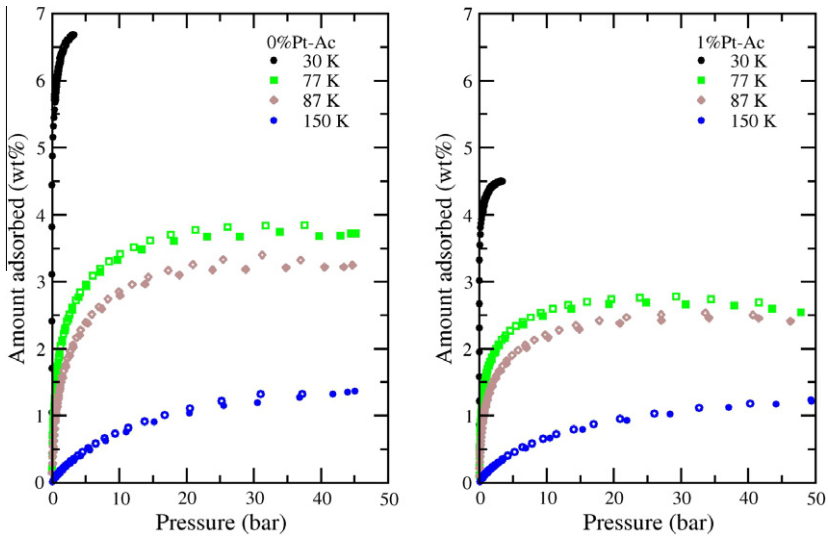

Fig. 5 – High-pressure excess hydrogen sorption isotherms for 0%Pt-Ac and 1%Pt-Ac at selected temperatures. At 77 K and 25 bar 0%Pt-Ac has a maximum excess adsorption of 3.7 wt.% while 1%Pt-Ac has 2.7 wt.%. Adsorption data are shown as filled symbols and desorption data as open symbols.

potential generated by the micro-pore walls cannot alone explain the adsorption heat enhancement in the Pt-containing carbons in our work. Considering the difference between our carbon samples and other carbons showing enhanced heat of adsorption [11–13,24,25], the reason for enhanced heat of adsorption in our carbons may lie in the Pt metal nanoparticle size and dispersion, templated structure, or how the carbon chemistry is involved with the platinum, which we will further elucidate below. It is apparent however that micropore size and volume are not the only factors affecting the heat of hydrogen adsorption.

3.6. *Surface chemistry of carbon containing different Pt loadings*

3.6.1. *Carbon surface composition by XPS analysis*

High resolution C1s core level spectra of the carbons were recorded and deconvoluted, in order of increasing binding energy, into seven components [26]: sp^2 and sp^3 hybridized carbon atoms, primary C—O (alcohols), epoxides or β-dihydroxy groups (denoted C—O—C), C=O (ketone) groups, and O=COR groups such as carboxyls and esters, and last are broad shake-up features attributed to π–π* transitions in the sp^2-hybridized carbons (Fig. 6). The most intense component in each of the spectra appears at a binding energy of about 285.0 eV, which is due to the graphitic, sp^2 hybridized carbons. The second component emerges at about 285.7 eV and was assigned as the sp^3 hybridized carbons, followed by a component close to 286.4 eV arising from the C—O groups. Summaries of the weight percentage of the different components in the carbons are in SI Table 1 (Cls) and SI Table 2 (Ols). The weight percentage of each C1s component is plotted against Pt loading in Fig. 6e. It is interesting to observe that in all the templated carbons, the carbon is primarily graphitic sp^2 hybridized carbon with tetrahedral sp^3 hybridized carbon being the second largest component. It is also worth noting

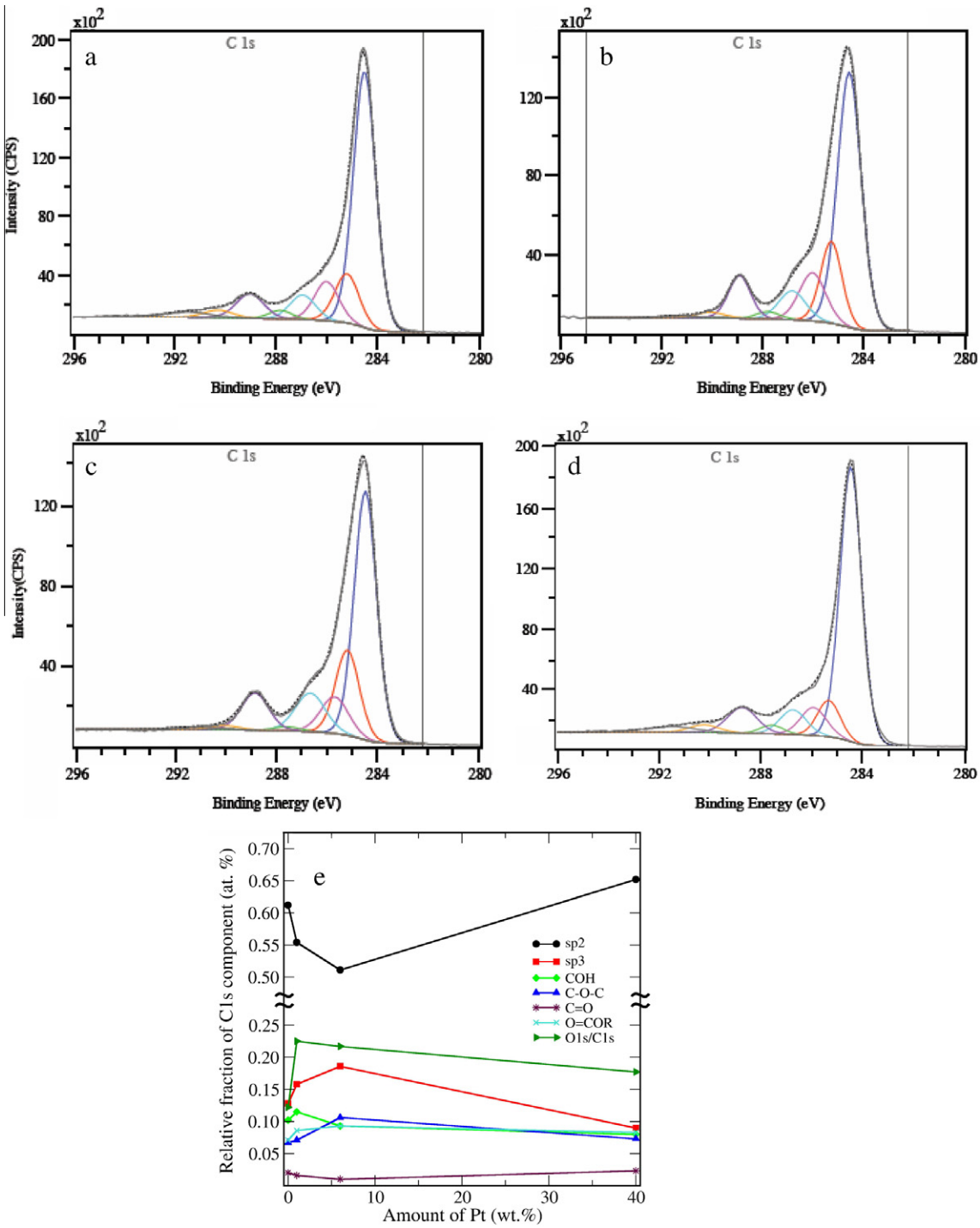

Fig. 6 – XPS analysis of the produced carbon samples: (a) 0%Pt-Ac, (b) 1%Pt-Ac, (c) 6%Pt-Ac, (d) 40%Pt-Ac, and (e) overall comparison of fraction of different components in the produced carbons.

the relative proportions of sp^2 and sp^3 carbon as a function of Pt loading. With increasing Pt loading, the sp^2 carbon amount first decreases when a low amount of Pt is present (less than 6 wt.%) and then increases. The precise value of Pt loading that correlates with a minimum sp^2 carbon level is not known and requires further experimentation. In contrast, an opposite trend was observed for the sp^3 hybridized carbon whose weight percentage increases with the Pt loading and reaches a maximum at about 6%Pt, for our range of materials, and then decreases with further increased Pt loading. Similar changes are seen in the different carbon—oxygen functionalities. With the exception of the C=O groups, the concentration of each functionality increases with initial Pt-loading, then decreases at higher loadings. Most components show an apparent peak for the 6%Pt-Ac sample, though the primary C—O groups peak at 1%Pt-Ac. The C=O feature, which is always a minor component (<2.5 at.%), decreases slightly with Pt-loading before increasing at high loadings. The general

trend for the individual carbon—oxygen functionalities agrees well with the bulk C/O ratio determined from survey scans, where the mass fraction of oxygen initially increases, reaching a peak for the 1%Pt-Ac sample, before slowly falling upon higher Pt-loading (Fig. 6e). It should also be noted that the platinum in all samples remains in the metallic Pt(0) state, showing no indication of oxidation in the Pt-4f core level spectra.

3.6.2. *Surface chemistry and influence on hydrogen adsorption*

We believe the differences in the carbon compositions are intimately related to the differences in the Pt-loaded parent zeolites. For the blank 0%Pt-Ac carbon, its parent template is NaY whose charge balancing ions are Na^+. For the carbons containing Pt nanoparticles, their parent templates are Pt $[(NH_3)_4](NO_3)_2$ impregnated NaY where some of the charge balancing ions Na^+ present in NaY were replaced by the $Pt[NH_3]_4^{2+}$ ions. The ion-exchange will change the framework acidity ultimately because $Pt[NH_3]_4^{2+}$ ions decompose to Pt nanoparticles during the pretreatment process, resulting in an increased framework acidity and facilitating isomerization and oligomerization of the acetylene gas molecules inside the zeolite channels during reduction [27]. If the Pt loading amount is small and the ion-exchanged $Pt[NH_3]_4^{2+}$ ion dominates as the charge balancing ions, acidic cracking dominates. Therefore, the more $Pt[NH_3]_4^{2+}$ ions, the less sp^2 carbon is produced compared to the bare template (NaY, which has no Pt at all), leading to our observation that the amount of sp^2 components in 1%Pt-Ac and 6%Pt-Ac gradually decreased while the amount of sp^3 components increased. However, when the Pt loading reaches 6 wt.%, which is theoretically approaching the ion-exchange capacity in the parent NaY zeolites, adding more Pt salt into the framework does not change the framework acidity but increases the size and amount of Pt nanoparticles produced during the reduction, leading to an increased graphitizing activity. Therefore, we observed that the sp^2 carbon percentage in the produced carbons increases with increased Pt loading amount. These phenomena are consistent with our analysis in (Section 3.2) for the size distribution of the Pt nanoparticles produced at different Pt loading amounts.

Since there is no evidence of a Pt-hydride forming at low temperatures and pressures, we believe the heat of adsorption enhancement observed in our work is not directly related to the presence of the platinum nanoparticles. Instead, we believe that the Pt salt plays an important role in affecting the surface oxidation level of the carbons. The observation that 1%Pt-Ac shows higher heat of adsorption at moderate uptakes than 0%Pt-Ac and 6%Pt-Ac coincides with the fact that 1%Pt-Ac sample has the highest mass fraction of oxygen, as well as of the primary C—O group, among all of the one-step produced carbons (Fig. 6e), suggesting a possible correlation between the enhanced hydrogen adsorption heat and the total surface concentration of oxygen species. While it would be tempting to attribute the enhanced isosteric heat to the presence of primary alcohols, further work would be needed to be definitive.

3.7. *Inelastic neutron scattering*

In order to further examine the local potential and self-diffusivity of hydrogen molecules/atoms in these templated microporous carbons, inelastic neutron scattering (INS) was used to investigate the hydrogen loading behavior in both the 0%Pt-Ac and 1%Pt-Ac samples. Fig. 7a illustrates the inelastic neutron scattering spectra obtained on the FANS spectrometer for H_2 loadings in 0%Pt-Ac in the range 0–2.0 wt.%, after subtraction of the bare material spectrum. Due to the large incoherent scattering cross section of hydrogen molecules, the measured

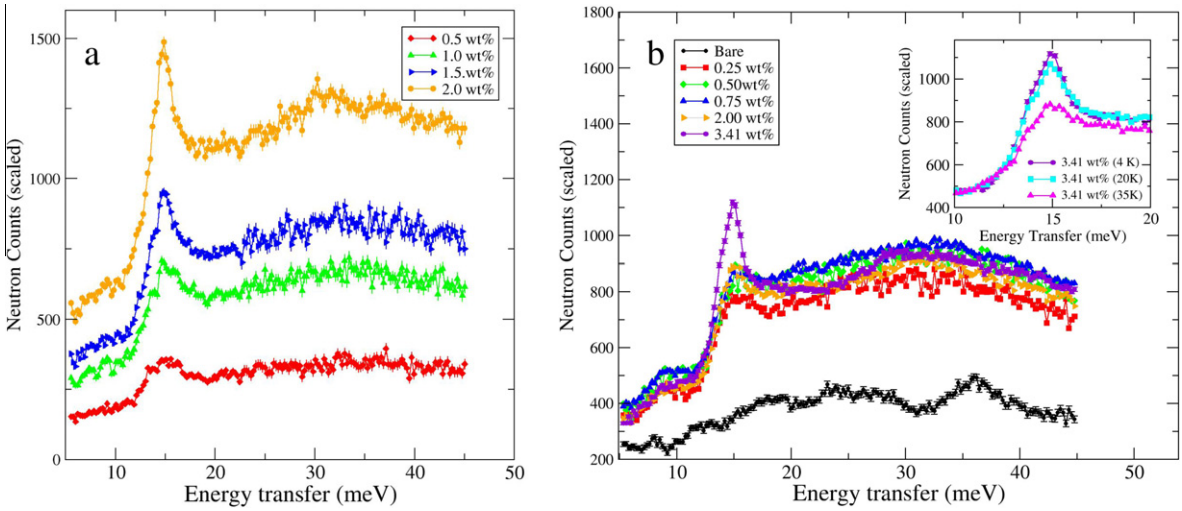

Fig. 7 – (a) Inelastic neutron spectra of 0%Pt-Ac and hydrogen measured on the FANS spectrometer at various H_2-loadings after subtracting the background spectrum. Error bars reflect one standard deviation in counting statistics. (b) INS spectra of 1%Pt-Ac H_2 loaded data are all proportionately scaled to 0.5 wt.% H_2 loading after subtracting the bare material spectrum (black symbols). Error bars are shown for the bare material and highest loading case and reflect one standard deviation in counting statistics. Effect of temperature on the H_2 rotational transition at the highest loading is shown in the inset of (b) to 35 K.

spectra contain the information of the localized movement of hydrogen molecules inside pores. At the lowest loading a very broad INS feature is located around the 14.7 meV expected for the rotational transition from the ground state to first excited state in free hydrogen. It could be possible that there is some fine structure in this peak (potentially measurable using a higher resolution instrument) that could be due to a raising of the rotational level degeneracy. The peak breadth could also result from a distribution of binding sites. Further loading sees a bulk H_2-like peak growing within this broad feature, and the concomitant growth in intensity of molecular recoil in the energy transfer range from 20 to 45 meV.

Fig. 7b shows INS spectra between 0 and 3.41 wt.% H_2 loading for 1%Pt-Ac. When scaled for the hydrogen content, the overall shapes of the curves are similar, save for some intensity changes in the hydrogen rotational peak at ca. 14.7 meV. Upon heating (Fig. 7b inset) there is a slight reduction in intensity to 20 K and a more substantial decrease by 35 K, while the overall shape and distribution of intensities are maintained. The lack of a very sharp intense rotational line and the persistent broad H_2 recoil spectrum indicates that the hydrogen adsorption potential is likely broad or flat-bottomed as a function of loading in this material, a conclusion consistent with the heats of adsorption deduced from the isotherms. In typical INS spectra from hydrogen adsorbed in carbon, one has a progression of hydrogen rotational lines, centered around ca. 14.7 meV, whose degeneracy may be lifted and yielding split peaks due to the adsorption potential or composed of multiple binding sites having differing rotational potentials [28–31]. With increased hydrogen loading a saturation of the strongest adsorption sites occurs with the appearance of a bulk-like singlet peak that usually is intense and proportional to the amount of less rotationally hindered or free H_2 in the pores. The current sample is somewhat different however, with little evidence of a strong bulk-like peak in the 1%Pt-Ac. Additionally, molecular recoil arises due to the lack of a restoring force when a neutron impinges on a hydrogen molecule and as such is an indication of relatively weak interactions between the H_2 and the substrate and is present in both samples from the lowest to highest loadings. We speculate that the unique morphological features of the templated carbon sample gives rise to this distribution of rotational intensity since the inter-connecting micro-channels in it are developed from the parent template resulting in a very peaked (< 2 nm) pore structure that is likely only correlated over very short distances. There are numerous studies that indicate the ideal slit-pore system for adsorption of hydrogen would be on the order of 6–9 A [31] and this would have a strong influence on the rotation hydrogen levels and the heat of adsorption. There is little evidence to indicate that such an ideal pore exists with sufficient quantity to influence the hydrogen rotational potential in these samples as probed using INS.

To further investigate structural influences on the transport phenomena of hydrogen molecules/atoms in the templated carbons, blank carbon without Pt loading, 0%Pt-Ac, was examined using the High-Flux Backscattering Spectrometer (HFBS). In fixed-window mode, the HFBS data for the bare 0%Pt-Ac material shows a linear decrease with increasing temperature proportional to the Debye–Waller factor (Fig. 8).

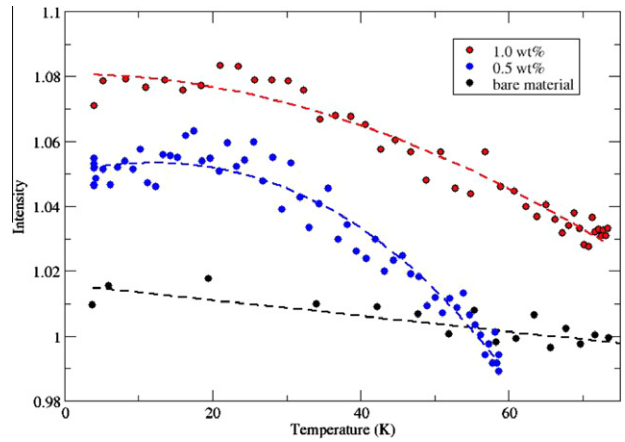

Fig. 8 – Fixed-window scans as a function of temperature of 0%Pt-Ac under two hydrogen-loading conditions. Data points are traced with dashed lines to guide the eye.

The addition of 0.5 wt.% hydrogen increases the total scattering measured in the detectors at the lowest temperatures, measuring the maximum amount of elastic scattering in the sample. As the system is warmed, the hydrogen becomes mobile on the timescale of the spectrometer, eventually moving faster than the ca. 10 ns timescale resolution of the instrument resulting in a decreased intensity that falls towards that of the bare material. At about 60 K all the hydrogen at 0.5 wt.% is moving faster than the instrument is capable of measuring but it is still adsorbed in the sample since no pressure in the experimental gas manifold is observed. For comparison a significant proportion is still moving on this relatively slow timescale for the 1 wt.% H_2 at 70 K. The apparent mobility of the hydrogen in this temperature range indicates that a neutron spectrometer such as the disk-chopper spectrometer (DCS) is most suitable to measure diffusion at the temperatures and hydrogen loadings of interest.

Quasi-elastic Neutron scattering (QENS) data measured on DCS for 0.5 wt.% hydrogen adsorbed in 0%Pt-Ac at various temperatures are shown in Fig. 9. The data at all temperatures except that of 30 K can be fitted over all momentum transfer (Q) groups using a fitting model of a delta-function, a broad Lorentzian and a narrow Lorentzian all convoluted with the instrumental resolution function. Literature data for QENS of hydrogen in several carbon-based materials from Grafoil [28], nanotubes [32] and XC-72 [33] report only this narrow component ascribed to mobile hydrogen; presumably the broader component seen here is absent in their data. However, hydrogen dynamics on two distinct timescales, albeit shorter than the ones measured here, have been observed in a potassium graphite intercalation compound [34] and by separate groups for an aluminosilicate zeolite [35,36]. The broad extra Lorentzian is clearly needed in our data as it dominates the spectra at 60 K, becoming less intense as the temperature is reduced and becomes indistinguishable from a linear background at 40 K. At 30 K there remains a small contribution to a Lorentzian, but data statistics and the low intensity make stable fits difficult to achieve using the small 0.15 $Å^{-1}$ Q-bins used for the other temperatures. The data and fits (delta and 2 Lorentzians) over a larger 1–2 $Å^{-1}$ Q-range

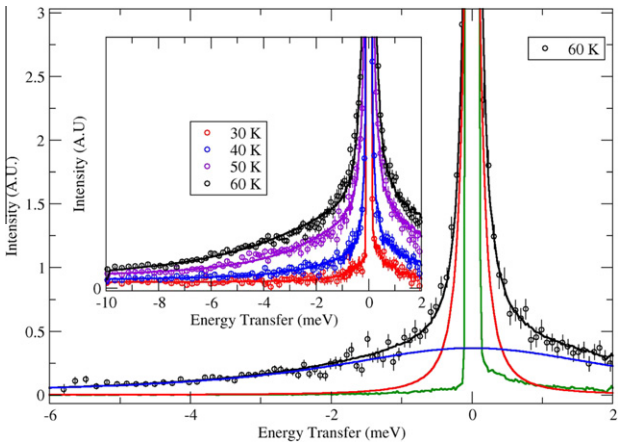

Fig. 9 – QENS data for 0.5 wt.% H_2 adsorbed on 0%Pt-Ac. The decomposition of the fit function is shown for the 60 K data at Q ca. 0.82 Å^{-1} (black circles), with the total curve as the black solid line (green: resolution function; red: narrow Lorentzian for adsorbed H_2; blue: broad Lorentzian). Inset shows the temperature dependence of the data (summed over 1–2 Å^{-1}) and the total fits as solid lines. Error bars are shown as vertical lines at the data points for 1 standard deviation. (For interpretation of the references to colour in this figure legend, the reader is referred to the web version of this article.)

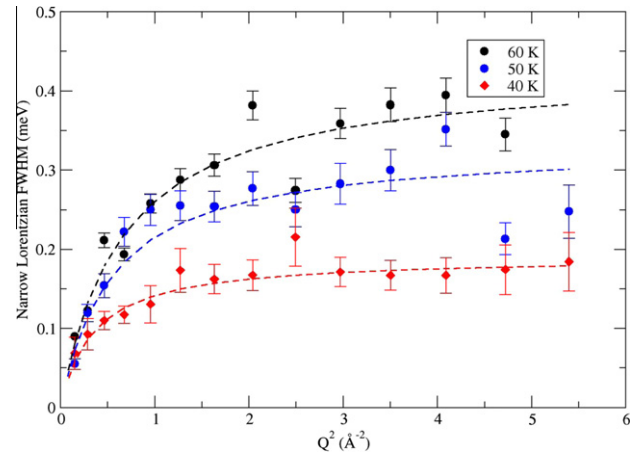

Fig. 10 – Full-width at half-maximum of the narrow Lorentzian for fits to the QENS data against Q^2. Dashed lines are fits to the data using a liquid-like jump diffusion model given in the text. Error bars indicate one standard deviation of the values from a least-squares fitting of the data to the phenomenological fit function.

is shown in the inset of the figure, where an elastic peak and a single moderately broad Lorentzian (FWHM = 1.8 ± 0.2 meV) and a background are required to fit the 30 K data.

Extraction of the pertinent fit parameters as a function of Q indicates that the static-hydrogen elastic intensity is dominated by strong small angle scattering peaking at about 0.5 Å^{-1}, consistent with a peak in the SAXS data, the intensity then falling with Q. There is very little difference in the stationary-H_2 elastic component in the 40–60 K temperature range, with only a small increase in intensity at higher-Q on cooling, reflecting a reduced Debye–Waller factor. The intensity of the narrow Lorentzian increases at small-Q and decays in a similar fashion as the elastic intensity, however the broad component almost linearly increases with Q.

The extracted line widths of the narrow component are distinctive, and as a function of Q^2, increase at low Q, and tend to an asymptote (Fig. 10). This behavior is characteristic of a jump-diffusion with no distinct spatial orientation of the jump direction as observed in other studies of H_2 in porous media [28,32,33]. The functional form expected for the FWHM in this liquid-like jump diffusion model is given in Eq. (2)

$$\mathrm{FWHM}(Q) = \frac{2\hbar}{\tau_0}\left(1 - \frac{1}{1 + Q^2 l_0^2}\right), \tag{2}$$

where the jump length, l, is assumed to have a distribution of values given by $l^* \exp(l/l_0)$, *where* l_0 is a characteristic jump length and τ_0 is a residency time at a site [37]. The effective self-diffusion coefficient can then be expressed as $D_{\mathrm{eff}} = l_0^2/\tau_0$. The FWHM data were fit to this model, yielding a characteristic jump length of 1.32 ± 0.07 Å at 60 K and similar for the lower temperatures. These values are close to those reported in other QENS studies of adsorbed hydrogen.

The residency times for hydrogen encapsulated by the narrow Lorentzian range from 6.2 ± 0.2, 4.0 ± 0.2, and 3.2 ± 0.1 ps at 40, 50 and 60 K, respectively. The resulting temperature dependent diffusion coefficients can then be fit to an Arrhenius Eq. (3):

$$D_{\mathrm{eff}} = D_0 e^{-E_{\mathrm{act}}/T}, \tag{3}$$

with a D_0 prefactor of $2.1(3) \times 10^{-8}$ m^2/s and an activation energy exponent, E_{act}, of 77 ± 9 K (640 ± 70 J/mol). The mobility of the hydrogen in the templated carbon is significantly reduced compared to H_2 at similar temperatures on nanotubes and on XC-72, and extrapolation of available data for HD on Grafoil (Fig. 11). Additionally, hydrogen mobility in all these systems is reduced from that of the bulk liquid measured by QENS [37] and extensively measured using NMR [38]. The activation energy for mobility at ca. 77 K, is significantly less than H_2 on nanotubes (135 ± 5 K), XC-72 (112 ± 5 K), or HD on Grafoil (145 ± 19 K), yet greater than that of bulk liquid (44.8 ± 1.6 K) [38]. These unusual characteristics for hydrogen in carbons presumably arise from the network of narrow pores in this zeolite-templated image of the zeolites and from the surface chemistry where the surface C—O functional groups possibly are providing the electrostatics to inhibit hydrogen mobility. In fact, the diffusion constants are extremely similar to those measured for zeolite 13X which exhibits dynamics characterized by $D_0 = 1.20(27) \times 10^{-8}$ m^2/s and E_{act} of 62 ± 11 K [36], though strong electrostatic interactions are presumably expected in the zeolite [36].

Having assigned the narrow Lorentzian to translational diffusion of hydrogen molecules associated with the pore walls in the carbon, we now speculate on the origins of the broader component. The intensity of the broader component, also fitted as a Lorentzian and characteristic of diffusion, continuously increases in the Q range covered in this experiment. It is difficult to ascertain the exact distribution of hydrogen ascribed to the narrow and broad components since the broad peak does not conform to a form-factor expected

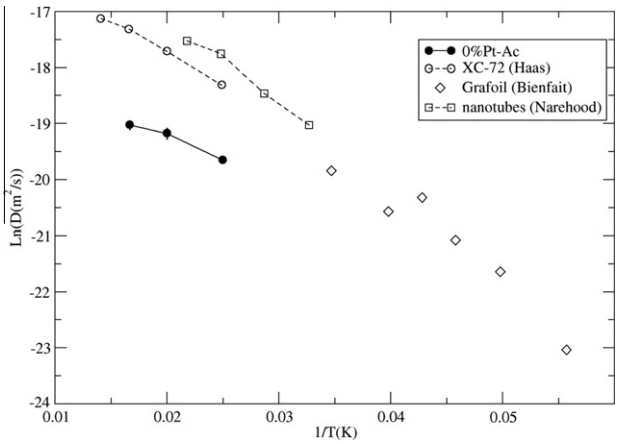

Fig. 11 – Natural log of the effective diffusion coefficient of hydrogen on select carbon substrates. Hydrogen in 0%Pt-Ac has a reduced mobility compared to that taken from single-walled nanotubes [32], Grafoil [28] or activated carbon XC-72 [33].

for Debye–Waller-damped zero-th order spherical Bessel function. At 50 K, the narrow peak reaches a maximum intensity of ca. 1.5, falling due to the Debye–waller factor to ca. 0.5 (arbitrary units) at the highest Q, compared to the broad Lorentzian that reaches ca. 4 (arbitrary units). As such we cannot extract meaningful information for this part of the data. A reasonable explanation of this behavior is the relatively small Q–ω range of the instrument compared to very fast hydrogen diffusion that has a very short jump distance. Since there is no over-pressure in the system, this component is not due to free hydrogen gas which moves too fast and, except for an elevated background level, would be too broad to observe on this spectrometer. Thus the broad Lorentzian component could imply the presence of a second fast moving Fickian- or fluid-like hydrogen within the pores that is weakly bound, an interpretation that is consistent with the rather broad INS features, significant recoil scattering and residency times as short as 0.1 ps (from the FWHM at high Q). Therefore, we postulate this fast hydrogen motion may be further linked to the interconnected channels present inside the templated carbon structure, which provide paths for even bulk-like hydrogen to diffuse through. Perhaps a logical extension of this description of differing hydrogen mobility is in the framework of the graphitic pore structures determined in the structure of templated carbons derived from zeolite NaY [39]. The slow hydrogen motion is almost certainly associated with the surface adsorption, while the occurrence of both narrow curved graphene-like channels with inner diameters of 9–13 Å and larger spherical bucky-bowl cavities (13–17 Å) could provide the space for the faster bulk-like diffusion.

4. Conclusion

We have successfully synthesised zeolite-templated microporous carbons containing dispersed Pt nanoparticles by using a smaller sized carbon precursor, acetylene, in our carbon templating work. The produced carbons have much better templated morphology than those developed in our previous 2-step work. Structural analysis using TEM, SAXS and XPS analysis reveal a well-developed bimodal dispersion of Pt nanoparticles, well-developed micro-channel arrays and indicate that the Pt loading amount affects not only the final structural replication but also the carbon composition. Hydrogen adsorption isotherms show that small micro-pores play a significant role in low pressure hydrogen adsorption capacities but the ultimate hydrogen adsorption capacity is still determined by the total micro-pore volume or surface area. Meanwhile, we have observed that platinum incorporation in the carbon slightly enhances the binding energy between hydrogen and the carbon adsorbent; 1%Pt-Ac and 6%Pt-Ac both show higher adsorption enthalpies than the blank 0%Pt-Ac sample. Our analysis has suggested that the carbon structure and surface chemistry may have played a significant role.

The local adsorption potential is probed using INS. With increased hydrogen loading, saturation of the strongest adsorption sites likely occurs with the appearance of a bulk-like rotational peak. The 1%Pt-Ac sample is somewhat different however, with little evidence of a strong bulk-like peak. Additionally, molecular recoil arises due to the lack of a restoring force when a neutron impinges on a hydrogen molecule and as such is an indication of relatively weak interactions and is present in both the blank and the Pt contained samples from the lowest to highest loadings.

QENS has shown that the hydrogen diffusion in the pores takes place on at least two time scales, simultaneously observed for the first time in a pure-carbon material. Dynamical studies show that hydrogen associated with the narrow pores or pore walls is less mobile than H_2 on typical carbons, and that this motion coexists with a much faster component. The activation energy for liquid-like hydrogen in the carbon is about 77 K, which is somewhat less than H_2 on adsorbed in other carbons. These unusual characteristics for hydrogen are believed to arise from the network of narrow pores in this zeolite-templated image of the zeolites as well as from surface chemical effects. In fact, the diffusion characteristics are extremely similar to those measured for zeolites 13X.

Acknowledgement

The authors are grateful for Jenny Fegent (CSIRO Publishing, Collingwood) for her helpful advices on paper writing. The support of the National Hydrogen Materials Alliance (NHMA) and Division of Earth Science and Resources Engineering of the Commonwealth Scientific Industrial Research Organisation (CSIRO), Australia is gratefully acknowledged – via a post-doctoral fellowship (to Yunxia Yang). The authors are also grateful for Monash University for providing financial support. XPS analysis was carried out at the Centre for Materials and Surface Science, La Trobe University. Work at NIST utilized facilities supported in part by the National Science Foundation under Agreement No. DMR-0454672 and was partially supported through the NIST Summer Undergraduate Research Fellowship (SURF) program and US DOE within the Hydrogen Sorption Center of Excellence. We thank Timothy Jenkins for technical assistance during the HFBS measurements.

Appendix A. Supplementary data

Supplementary data associated with this article can be found, in the online version, at doi:10.1016/j.carbon.2010.11.050.

REFERENCES

[1] Han SJ, Hyeon T. Novel silica-sol mediated synthesis of high surface area porous carbons. Carbon 1999;37(10):1645–7.
[2] Han SJ, Hyeon T. Simple silica-particle template synthesis of mesoporous carbons. Chem Commun 1999(19):1955–6.
[3] Schuth F, Schmidt W. Microporous and mesoporous materials. Adv Mater 2002;14(9):629–38.
[4] Wan Y, Zhao DY. On the controllable soft-templating approach to mesoporous silicates. Chem Rev 2007;107(7):2821–60.
[5] Hou PX, Yamazaki T, Orikasa H, Kyotani T. An easy method for the synthesis of ordered microporous carbons by the template technique. Carbon 2005;43(12):2624–7.
[6] Wu ZX, Yang YX, Gu D, Zhai YP, Feng D, Li Q, et al. Synthesis of ordered mesoporous carbon materials with semi-graphitized walls via direct in-situ silica-confined thermal decomposition of CH_4 and their hydrogen storage properties. Top Catal 2009;52(1–2):12–26.
[7] Yang YX, Singh RK, Webley PA. Hydrogen adsorption in transition metal carbon nano-structures. Adsorption J Int Ads Soc 2008;14(2–3):265–74.
[8] Yang YX, Bourgeois L, Zhao CX, Zhao DY, Chaffee A, Webley PA. Ordered micro-porous carbon molecular sieves containing well-dispersed platinum nanoparticles for hydrogen storage. Micropor Mesopor Mater 2009;119(1–3):39–46.
[9] Kyotani T. Control of pore structure in carbon. Carbon 2000;38(2):269–86.
[10] Nishihara H, Hou PX, Li LX, Ito M, Uchiyama M, Kaburagi T, et al. High-pressure hydrogen storage in zeolite-templated carbon. J Phys Chem C 2009;113(8):3189–96.
[11] Yushin G, Dash R, Jagiello J, Fischer JE, Gogotsi Y. Carbide-derived carbons: effect of pore size on hydrogen uptake and heat of adsorption. Adv Funct Mater 2006;16(17):2288–93.
[12] Yang Z, Xia Y, Mokaya R. Enhanced hydrogen storage capacity of high surface area zeolite-like carbon materials. J Am Chem Soc 2007;129(6):1673–9.
[13] Zhou W, Wu H, Hartman MR, Yildirim T. Hydrogen and methane adsorption in metal-organic frameworks: a high-pressure volumetric study. J Phys Chem C 2007;111(44):16131–7.
[14] Spalla O, Lyonnard S, Testard F. Analysis of the small-angle intensity scattered by a porous and granular medium. J Appl Crystallogr 2003;36:338–47.
[15] Beaucage G. Approximations leading to a unified exponential power-law approach to small-angle scattering. J Appl Crystallogr 1995;28:717–28.
[16] Beaucage G, Schaefer DW. Structural studies of complex-systems using small-angle scattering – a unified guinier power-law approach. J Non-Cryst Solids 1994;172:797–805.
[17] Glatter O, Kratky O. Small angle X-ray scattering. London: Academic Press, Inc.; 1982.
[18] Udovic TJ, Brown CM, Leao JB, Brand PC, Jiggetts RD, Zeitoun R, et al. The design of a bismuth-based auxiliary filter for the removal of spurious background scattering associated with filter-analyzer neutron spectrometers. Nucl Instrum Methods A 2008;588(3):406–13.
[19] Meyer A, Dimeo RM, Gehring PM, Neumann DA. The high-flux backscattering spectrometer at the NIST center for neutron research. Rev Sci Instrum 2003;74(5):2759–77.
[20] Copley JRD, Cook JC. The Disk Chopper Spectrometer at NIST: a new instrument for quasielastic neutron scattering studies. Chem Phys 2003;292(2–3):477–85.
[21] Azuah RT, Kneller LR, Qiu YM, Tregenna-Piggott PLW, Brown CM, Copley JRD, et al. DAVE: a comprehensive software suite for the reduction, visualization, and analysis of low energy neutron spectroscopic data. J Res Natl Inst Stand Technol 2009;114(6):341–58.
[22] Gogotsi Y, Dash RK, Yushin G, Yildirim T, Laudisio G, Fischer JE. Tailoring of nanoscale porosity in carbide-derived carbons for hydrogen storage. J Am Chem Soc 2005;127(46):16006–7.
[23] Gogotsi Y, Portet C, Osswald S, Simmons JM, Yidirim T, Laudisio G, et al. Importance of pore size in high-pressure hydrogen storage by porous carbons. Int J Hydrogen Energ 2009;34(15):6314–9.
[24] Lachawiec Jr AJ, Yang RT. Isotope tracer study of hydrogen spillover on carbon-based adsorbents for hydrogen storage. Langmuir 2008;24:6159–65.
[25] Li YW, Yang RT. Hydrogen storage on platinum nanoparticles doped on superactivated carbon. J Phys Chem C 2007;111(29):11086–94.
[26] Briggs D, Beamson G. Primary and secondary oxygen-induced C1s binding energy shifts in X-ray photoelectron-spectroscopy of polymers. Anal Chem 1992;64(15):1729–36.
[27] Chen L, Singh RK, Webley P. Synthesis, characterization and hydrogen storage properties of microporous carbons templated by cation exchanged forms of zeolite Y with propylene and butylene as carbon precursors. Micropor Mesopor Mater 2007;102(1–3):159–70.
[28] Bienfait M, Zeppenfeld P, Ramos RC, Gay JM, Vilches OE, Coddens G. Isotopic ordering in adsorbed hydrogen monolayers. Phys Rev B 1999;60(16):11773–82.
[29] Fernandez-Alonso F, Bermejo FJ, Cabrillo C, Loutfy RO, Leon V, Saboungi ML. Nature of the bound states of molecular hydrogen in carbon nanohorns. Phys Rev Lett 2007;98(21):4.
[30] Georgiev PA, Ross DK, Albers P, Ramirez-Cuesta AJ. The rotational and translational dynamics of molecular hydrogen physisorbed in activated carbon: a direct probe of microporosity and hydrogen storage performance. Carbon 2006;44(13):2724–38.
[31] Wang QY, Johnson JK. Molecular simulation of hydrogen adsorption in single-walled carbon nanotubes and idealized carbon slit pores. J Chem Phys 1999;110(1):577–86.
[32] Narehood DG, Pearce JV, Eklund PC, Sokol PE, Lechner RE, Pieper J, et al. Diffusion of H_2 adsorbed on single-walled carbon nanotubes. Phys Rev B 2003;67(20):5.
[33] Haas OE, Simon JM, Kjelstrup S, Ramstad AL, Fouquet P. Quasi-elastic neutron scattering investigation of the hydrogen surface self-diffusion on polymer electrolyte membrane fuel cell catalyst support. J Phys Chem C 2008;112(8):3121–5.
[34] Purewal JJ, Keith JB, Ahn CC, Fultz B, Brown CM, Tyagi M. Adsorption and melting of hydrogen in potassium-intercalated graphite. Phys Rev B 2009;79(5):7.
[35] Fu H, Trouw F, Sokol PE. A quasi-elastic and inelastic neutron scattering study of H-2 in zeolite. J Low Temp Phys 1999;116(3–4):149–65.
[36] DeWall J, Dimeo RM, Sokol PE. Slow diffusion of molecular hydrogen in zeolite 13X. J Low Temp Phys 2002;129(3–4):171–84.
[37] Egelstaff PA. An introduction to the liquid state. New York: Academic Press; 1967.
[38] Oreilly DE, Peterson EM. Self-diffusion of liquid-hydrogen and deuterium. J Chem Phys 1977;66(3):934–7.
[39] Nishihara H, Yang QH, Hou PX, Unno M, Yamauchi S, Saito R, et al. A possible buckybowl-like structure of zeolite templated carbon. Carbon 2009;47(5):1220–30.